Membrane-Free Electrochemical Production of Acid and Base Solutions Capable of Processing Ultramafic Rocks

Benjamin P. Charnay[1†], Yuxuan Chen[1†], Rishi G. Agarwal[1†], Jason W. Misleh[1], J. Gage Wright[1], Ethan R. Sauvé[2], Wei Lun Toh[2], Yogesh Surendranath[2*], Matthew W. Kanan[1*]

[1]Department of Chemistry, Stanford University, 337 Campus Drive, Stanford, 94305, CA, USA.
[2]Department of Chemistry, Massachusetts Institute of Technology, 77 Massachusetts Ave., Cambridge, 02139, MA, USA.

*Corresponding author(s). E-mail(s): yogi@mit.edu; mkanan@stanford.edu;
Contributing authors: benchy@stanford.edu; yuxuanc@stanford.edu; co2rishi@stanford.edu; jwmisleh@stanford.edu; jgwright@stanford.edu; esauve@mit.edu; wltoh@mit.edu;
†These authors contributed equally to this work.

Abstract

Chemical transformations that are effected by sequential addition of acid and base can be performed in closed-loop processes powered by electricity if the acid and base are produced electrochemically from water. Conventional methods of electrochemical acid-base production utilize ion exchange membranes (IEMs) to inhibit proton (H^+) and hydroxide (OH^-) recombination, but these components lead to high resistive losses, low current densities, and poor tolerance for polyvalent metal ions, which compromise energy efficiency and scalability. Here we use an ion transport model to guide the design of an acid-base co-generating system that inhibits recombination via competitive transport of the supporting electrolyte and masking H^+ as HSO_4^-, which enables the use of a simple porous separator instead of IEMs. Using the H_2 oxidation reaction (HOR) and H_2 evolution reaction (HER) for H^+ and OH^- production, we demonstrate steady-state co-generation of acid and base solutions at useful concentrations in the presence of polyvalent impurities with lower energy demand and higher current density than

https://doi.org/10.26434/chemrxiv-2023-5tndz **ORCID:** https://orcid.org/0000-0003-2327-2511 Content not peer-reviewed by ChemRxiv. **License:** CC BY-NC-ND 4.0

state-of-the-art reported IEM-based systems. Cells can be stacked by combining HER and HOR electrodes into a bipolar gas diffusion electrode, which recirculates H_2 with near-unity efficiency. The acid and base outputs of the cell are capable of extracting alkalinity from olivine and serpentine in the form of $Mg(OH)_2$ and $Mg(OH)_2 \cdot 2\,MgSiO_3$, which are shown to be competent for removing CO_2 from dilute streams to form Mg carbonates.

Introduction

Chemical transformations that are critical to carbon management and sustainable resource utilization can be driven by the sequential application of aqueous acidic and basic solutions(*1*, *2*). For example, CO_2 can be concentrated from dilute sources by capturing it as (bi)carbonate with base and releasing it with acid. $CaCO_3$ can be converted to slaked lime ($Ca(OH)_2$) at ambient temperature by sequential protonation to form soluble Ca^{2+} and basic precipitation. Similarly, the extraction and purification of metal ions from natural resources or waste products can be achieved by sequential acid leaching and basic precipitation. Extracting $Mg(OH)_2$ from ultramafic rocks by acid-base processing could be used to remove CO_2 from the atmosphere and permanently store it as Mg carbonates (*3*, *4*). Carrying out these pH-swing transformations at scale without stoichiometric waste requires efficient and sustainable methods to generate acid and base from water.

Renewable electricity can be used to drive the dissociation of water into H^+ and OH^-, either at electrodes that carry out acid- and base-generating electrocatalytic half-reactions or at the junction of cation and anion exchange membrane components of a bipolar membrane (BPM)(*5*). A major source of efficiency loss is deleterious recombination of H^+ and OH^- before they are removed from the cell by flowing electrolyte or utilized in productive chemistry. Recombination is a particularly pernicious problem because the diffusion coefficients of H^+ and OH^- greatly exceed that of all other cations and anions in water due to rapid Grotthuss hopping(*6*). Traditionally, this problem is mitigated by incorporating one or more ion-exchange membranes (IEMs) between the acid and base compartments (Fig.1A). Cation-exchange membranes (CEMs) serve to inhibit OH^- transport, whereas anion exchange membranes (AEMs) serve to inhibit H^+ transport. The commercial technology for acid-base co-generation, bipolar membrane electrodialysis (BPMED), combines both modes of inhibition by utilizing a stack consisting of a CEM, AEM, and bipolar membrane (BPM) (Fig.1B). BPMED has been employed for many years in specialty chemical processes (*5*, *7*). More recently, proof-of-concept studies have described the use of IEM-based acid-base co-generation for CO_2 capture from flue gas (*8*) and seawater (*9*), the conversion of limestone ($CaCO_3$) and H_2O into $Ca(OH)_2$ and CO_2 (*10*, *11*), and the conversion of gypsum ($CaSO_4$) and H_2O into $Ca(OH)_2$ and H_2SO_4(*12*, *13*).

Notwithstanding these precedents, the reliance on IEMs presents a substantial impediment to large-scale application of acid-base co-generation in carbon management and sustainable resource utilization. The narrow ion channels of an IEM restrict ionic current flow, thereby introducing substantial resistive losses even at modest current densities. Furthermore, cation-exchange membranes (CEMs) become much more

https://doi.org/10.26434/chemrxiv-2023-5tndz **ORCID:** https://orcid.org/0000-0003-2327-2511 Content not peer-reviewed by ChemRxiv. **License:** CC BY-NC-ND 4.0

resistive in the presence of polyvalent cations (e.g. Ca^{2+}, Mg^{2+}, transition metal ions, etc.) and can be irreversibly damaged by precipitation of polyvalent hydroxides or carbonates in their channels (*14*). Consequently, the NaCl solutions used in CEM-based chloro-alkali technologies must be scrubbed of polyvalent ions to low parts per billion levels to prolong membrane lifetimes (*15*). Since most potential applications of acid-base co-generation involve resources with high polyvalent cation content (e.g. $CaCO_3$, $CaSO_4$, ultramafic rocks, seawater), the use of CEMs would require extensive pre-scrubbing. AEMs tolerate polyvalent cations, but most AEMs do not block H^+ transport very well and/or are incompatible with alkaline electrolytes(*16*). An advanced H^+ blocking AEM could address this problem but would incur even larger resistive losses(*17*).

We hypothesized that efficient acid-base co-generation could be achieved without IEMs by using the supporting electrolyte to out-compete H^+ and OH^- transport and mask H^+ as a low-pKa anion (Fig.1C). This approach enables the use of a simple porous diaphragm to separate the acid and base streams, which greatly reduces the ionic resistance and removes the polyvalent intolerance imposed by IEMs. Herein, we develop a transport model that predicts the effect of competitive electrolyte migration on the efficiency of electrochemical acid-base co-generation. Guided by this model, we design a simple 2-compartment cell that generates acid and base solutions at useful concentrations (up to 1.275 M) with efficiencies exceeding the state-of-the-art membrane electrodialysis systems and that tolerates polyvalent cation impurities. Optimal performance is achieved by using mixed electrolytes in which Cl^- is employed to out-compete OH^- transport and SO_4^{2-} binds H^+ as HSO_4^-. To minimize the cell potential, we utilize the H_2 oxidation reaction (HOR) and H_2 evolution reaction (HER) for H^+ and OH^- generation, respectively(*18–20*). By combining HOR and HER gas diffusion electrodes (GDEs) into a bipolar gas diffusion electrode (BPGDE), we show that cells can be combined into a stack such that H_2 produced by HER is consumed by HOR with near-unity efficiency (Fig.1D).

To demonstrate the utility of the acid and base solutions generated by the cell, we use them to perform closed-loop processes that extract $Mg(OH)_2$ and $Mg(OH)_2 \cdot 2\,MgSiO_3$ from olivine and serpentine, respectively. In sharp contrast to the inertness of olivine and serpentine, these materials carbonate rapidly under 1 atm CO_2 in an aqueous suspension to form $Mg(HCO_3)_2$. We also show that the $Mg(OH)_2$ extracted from olivine carbonates under wet conditions in ambient air within 8 months to form magnesite ($MgCO_3 \cdot 3\,H_2O$). The approach demonstrated here enables the use of electrochemical acid-base generation to drive key chemical transformations in carbon management and sustainable resource utilization.

Acid-Base Generating Cell Design, Modeling, and Performance

To evaluate our strategy for acid-base generation, we fabricated a cell consisting of two flowing electrolyte compartments separated by a porous diaphragm (Zirfon) and two gas diffusion electrodes (GDEs) (Fig. 2A and fig. S1). Each electrolyte compartment was assembled out of a series of gaskets such that the thickness of the flowing anolyte and catholyte layers is only 375 μm, which reduces solution resistance. A GDE with a Pt/C catalyst layer was used for the anode and one with a PtNi/C catalyst layer was used for the cathode because of their superior performance for HOR and

https://doi.org/10.26434/chemrxiv-2023-5tndz **ORCID:** https://orcid.org/0000-0003-2327-2511 Content not peer-reviewed by ChemRxiv. **License:** CC BY-NC-ND 4.0

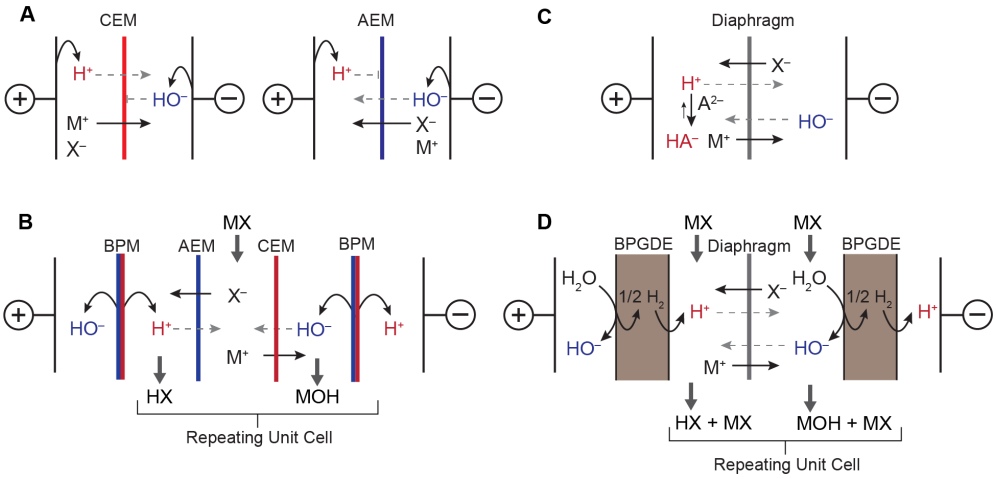

Fig. 1 Comparison of approaches to generating acid and base solutions. (**A**) Conventional acid-base generating schemes that use either a CEM to inhibit HO^- crossover (left) or an AEM to inhibit H^+ crossover (right). (**B**) Schematic of a BPMED system, which uses a BPM to dissociate H_2O into H^+ and OH^- and a combination of a CEM and AEM to generate separate acid and base streams. (**C**) Acid-base generation using a diaphragm separator instead of IEMs. Suppressing recombination relies on out-competing H^+ and OH^- transport with excess electrolyte ions and "masking" H^+ as a low-pKa anion. (**D**) Design for a IEM-free stack using a BPGDE to generate H^+ and OH^- by HOR and HER, respectively.

HER and their use in large-scale industrial processes(*21*). The use of GDEs facilitates H_2 transport to the anode catalyst and clears H_2 efficiently at the cathode to prevent bubble formation.

Acid-base generation with this cell is performed by flowing electrolyte through the two compartments at a fixed volumetric rate per electrode area (Q) while applying a fixed total current density (j_{tot}) and supplying the anode with H_2. To simplify the operation of the cell for our initial experiments, H_2 was supplied to the anode from an external source rather than using the cathodic H_2. The ability to recirculate the H_2 produced by the cathode for consumption at the anode at high efficiency was demonstrated for a stack configuration (see below).

The key performance metrics for electrochemical acid-base co-generation are the current density for productive acid and base generation (j_p), the energy demand per mol of acid and base generated (E_{ab}), the concentration of the acid and base outputs (C_{H^+} and C_{OH^-}), and the stability of the system over time and to the impurities in the input salt solution. j_p is given by Equation 1:

$$j_p = j_{tot} * CE \tag{1}$$

where CE is the current efficiency, which is the percentage of the current that results in productive acid and base generation. 100% CE corresponds to zero recombination

https://doi.org/10.26434/chemrxiv-2023-5tndz **ORCID:** https://orcid.org/0000-0003-2327-2511 Content not peer-reviewed by ChemRxiv. **License:** CC BY-NC-ND 4.0

of H^+ and OH^-. E_{ab} is determined by Equation 2:

$$E_{ab} = \frac{V_{cell} * F * 100}{CE} \tag{2}$$

where V_{cell} is the measured steady-state cell voltage and F is Faraday's constant. V_{cell} includes the thermodynamic voltage and resistive losses (iR) as well as the HOR and HER overpotentials. V_{cell} and CE can also be used to calculate the energy efficiency (EE) according to Equation 3:

$$EE = \frac{0.0592 \Delta pH * CE}{V_{cell} * 100} \tag{3}$$

where $0.0592 * \Delta pH$ is the thermodynamic minimum cell voltage for a given pH difference between the output acidic and basic solutions. Finally, C_{H^+} and C_{OH^-} are determined by Equation 4:

$$C_{H^+} = \frac{j_p}{Q * F} \tag{4}$$

Note that $C_{H^+} = C_{OH^-}$ if the anolyte and catholyte flow rates are the same.

Since acid-base generation with this design relies on out-competing H^+ and OH^- transport with other ions, the composition of the electrolyte is critical to maximizing CE. We focused on electrolytes made from NaCl and Na_2SO_4 because these salts are the most abundant and lowest cost choices. With pure NaCl electrolyte, acid is generated exclusively as H_3O^+ (Fig. 2A). While H_3O^+ is the strongest possible acid in H_2O, its very high mobility is expected to negatively impact CE. With SO_4^{2-}-containing electrolytes, electrogenerated H^+ can be masked as HSO_4^-, which is a weaker acid than H_3O^+ (pKa 2 vs. pKa 0) but still strong enough to leach cations from ultramafic rocks (see below). Since HSO_4^- must oppose the electric field to cross the separator and has a relatively low diffusion coefficient, the use of SO_4^{2-} is expected to improve CE(*22*).

To guide optimization of the electrolyte composition and gain insight into the physicochemical phenomena that affect cell performance, we developed a model that predicts the steady state concentration of all the ions in the catholyte and anolyte streams for a given electrolyte composition and j_{tot}/Q ratio. The model functions by employing a damped fixed-point iteration process to simultaneously solve the coupled equations that describe ion transport, acid-base and ion-pairing equilibria, and the deviations from ideality captured by the activity coefficients (γ) (see Supplementary Matterials Section Model Design). Since j_{tot}/Q determines the concentration of H^+ and OH^- generated by the electrodes and the model calculates the transport of all the ions, the model directly predicts the steady-state acid and base concentrations (C_{H^+} and C_{OH^-}), which can be used to calculate the predicted j_p and CE by Equations 4 and 1. Note that C_{H^+} includes both the H_3O^+ and HSO_4^- concentrations.

Acid-base generation with our cell was first evaluated by performing a series of short (15-90 min) runs at variable j_{tot} (50-500 mA cm^{-2}) using fixed Q (0.1 mL min^{-1} cm^{-2} for both anolyte and catholyte) with three different electrolytes: 3 M NaCl, 0.75 M Na_2SO_4, and 3 M NaCl + 0.75 M Na_2SO_4. For each experiment, the steady-state

https://doi.org/10.26434/chemrxiv-2023-5tndz **ORCID:** https://orcid.org/0000-0003-2327-2511 Content not peer-reviewed by ChemRxiv. **License:** CC BY-NC-ND 4.0

V_{cell} was measured and C_{OH^-} (which is equivalent to C_{H^+}) was determined by using the output catholyte to precipitate $Mg(OH)_2$ from a 2 M solution of $MgCl_2$ and then isolating and weighing the $Mg(OH)_2$. The C_{OH^-} was used to calculate CE and j_p and then CE and V_{cell} were used to calculate E_{ab} and EE according to Equations 2 and 3, respectively.

Fig. 2B shows the predicted and experimental values for CE as j_{tot} was varied. The x-axis is the ratio j_{tot}/QF, which has units of concentration corresponding to the output acid and base concentrations that would be attained if CE were 100%. The predicted curves showed good quantitative agreement with the data for both the pure NaCl and mixed NaCl+Na_2SO_4 electrolytes, and only a slight offset for the pure Na_2SO_4 electrolyte. The CE increases in the order Na_2SO_4 < NaCl < mixed NaCl+Na_2SO_4 electrolyte, with an unexpectedly large benefit afforded by the mixed electrolyte.

The model provides insight to explain the electrolyte-dependence of CE by revealing the current contributions of each ion (fig. S2). Fig. 2C shows the contributions of H^+ and OH^- crossover to the loss in CE as a function of j_{tot}/QF. (H^+ crossover includes both H_3O^+ and HSO_4^- for the Na_2SO_4-containing electrolytes). With the NaCl electrolyte, H_3O^+ crossover is the major source of CE degradation, accounting for ~27% CE loss at 50 mA cm^{-2} and rising to 60% at 500 cm^{-2}, while OH^- crossover accounts for only 5% and 11%, respectively. Upon switching to pure Na_2SO_4, H_3O^+ transport is attenuated by the formation of HSO_4^-. The ability of this electrolyte to mitigate H^+ crossover is limited, however, because a substantial portion of the SO_4^{2-} ions are masked as $NaSO_4^-$ ion pairs (fig. S2) and there is also a small amount of diffusive crossover of HSO_4^-. Because of the lower mobility and lower concentration of $NaSO_4^-$(*23*) compared to Cl^-, there is substantially greater OH^- crossover from the catholyte in Na_2SO_4 vs. the NaCl electrolyte, which more than offsets the difference in H^+ crossover and thereby leads to lower CE.

In the case of the mixed electrolyte, OH^- crossover is mitigated by the supporting Cl^- as compared to the pure Na_2SO_4 electrolyte. More strikingly, the H^+ crossover is reduced compared to both the NaCl and Na_2SO_4 electrolytes much more than would be expected from simply having a higher Na^+ concentration in the anolyte (except at the highest j_{tot}, where it is the same for the mixed and Na_2SO_4 electrolytes). The model reveals that this outsized benefit arises because γ >1 for H_3O^+ and γ <1 for all other species in this highly non-ideal electrolyte. As a result, HSO_4^- formation increases and $NaSO_4^-$ decreases, which reduces H^+ crossover and improves CE.

Key performance metrics of the acid-base generating cell across the three electrolytes are summarized in Fig. 2D, which shows the E_{ab} and EE values, and Fig. 2E, which shows the j_p the output C_{H^+} and C_{OH^-} values over the j_{tot} range of 50-500 mA cm^{-2}. V_{cell} values are provided in table S2. The mixed electrolyte showed the best performance, generating acid and base at concentrations ranging from 0.26 to 1.25 M with the corresponding E_{ab} of 0.03 to 0.116 kWh mol^{-1} and j_p of 42 to 206 mA cm^{-2}. The E_{ab} values correspond to V_{cell} values of 0.93 V to 1.79 V and EE values of 64% to 19%. Although EE is highest for the mixed electrolyte, the V_{cell} values are actually lower for the NaCl electrolyte, which may arise from the lower viscosity and the higher free H_3O^+ concentration in the anolyte for the NaCl electrolyte.

https://doi.org/10.26434/chemrxiv-2023-5tndz **ORCID:** https://orcid.org/0000-0003-2327-2511 Content not peer-reviewed by ChemRxiv. **License:** CC BY-NC-ND 4.0

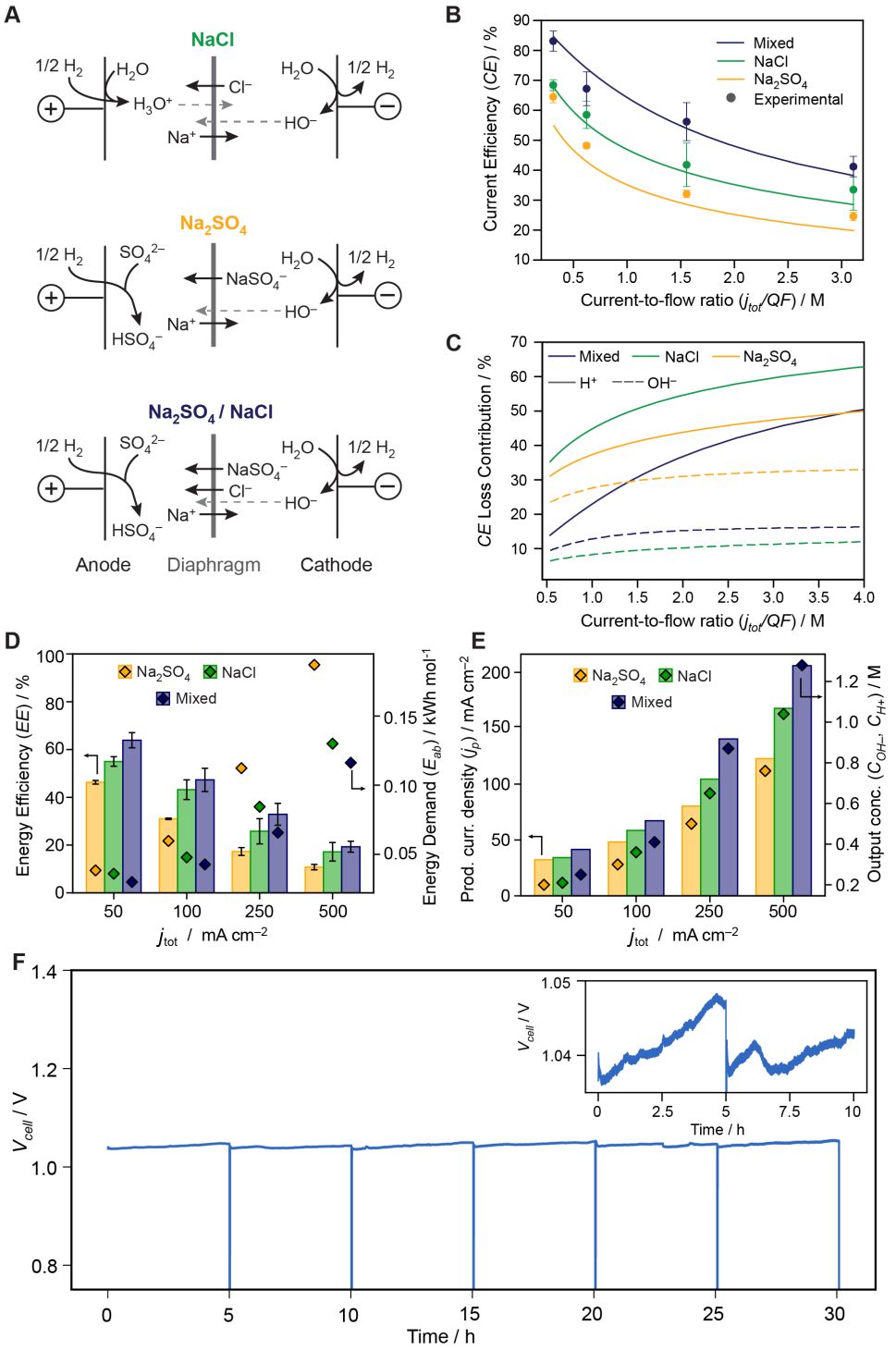

Fig. 2 Design and performance of membrane-free acid-base co-generating electrochemical cell (**A**) Ion transport schemes for 3 different electrolytes. (**B**) Model and validation of current efficiency at different current-to-flow ratios. (**C**) Contributions of H^+ and OH^- to the loss of current efficiency as a function of the current to flow ratio. (**D**) Energy demand and energy efficiency values for a range of j_{tot} at a constant $Q = 0.1$ mL min^{-1}. (**E**) Corresponding values for productive current density and output acid and base concentrations. (**F**) Cell voltage vs. time trace for a 30 h run at $j_{tot} = 100$ mA cm^{-2} and $Q = 0.1$ mL min^{-1} cm^{-2} in mixed NaCl/Na_2SO_4 electrolyte containing Mg and Si impurities. The cell was operated in reverse polarity for 60 s every 5 h. The average V_{cell} is 1.04 V. V_{cell} decays by 1-2 mV h^{-1} (inset), but it is recovered by brief reverse polarization.

https://doi.org/10.26434/chemrxiv-2023-5tndz **ORCID:** https://orcid.org/0000-0003-2327-2511 Content not peer-reviewed by ChemRxiv. **License:** CC BY-NC-ND 4.0

To assess stability, the two-compartment cell was operated in longer runs using mixed NaCl+Na_2SO_4 electrolyte that had been used to process ultramafic rocks (see below). This recycled electrolyte was found to contain ∼300 µM each of Mg and Si impurities by ICP-OES (table S4). At j_{tot} = 100 mA cm^{-2} and Q = 0.1 mL min^{-1} cm^{-2}, V_{cell} exhibited a steady increase of ∼1 mV h^{-1}. We hypothesized that this voltage decay is the result of scale deposits on the cathode from precipitation of $Mg(OH)_2$ or SiO_2 as base is generated. One method that is used effectively to reverse voltage decay from small scale deposits in industrial saline concentrating stacks is to periodically apply a brief reverse polarization to generate acid that dissolves the deposits (*24*). We therefore used a duty cycle where the cell was operated in reverse polarity at the same j_{tot} for 60 s every 5 h. The net current passed is 99.7% of that which would have been passed over the same time span without the reverse polarization duty cycle. As seen in Fig. 2F, reverse polarization repeatedly restored the voltage decay that occurred over each 5 h period, demonstrating that this strategy is viable for maintaining efficiency in long-term operation of the cell. The average voltage restoration after every step was 6 mV ± 1 mV with individual steps having a decay rate of 1.6 mV h^{-1} ± 0.4 mV h^{-1}. The CE measured by $Mg(OH)_2$ precipitation was 65%, agreeing with the value predicted by the model (71%).

The performance summarized in Fig.2 demonstrates that our strategy for acid-base production can achieve energy efficiency, throughput, and impurity tolerance that rival or exceed state-of-the-art IEM-based systems. In the commercial BPMED technology, a stack of cells composed of an AEM, a CEM, and a BPM convert a concentrated salt solution into acid and base solutions along with a depleted salt solution (Fig. 1A) (*5*, *7*). In the best performance reported to date, a BPMED system operated with an E_{ab} ranging from 0.073 to 0.145 kWh mol^{-1} at j_p of only ≈ 30 mA cm^{-2} to generate solutions ranging from 0.6 - 2.1 M (*25*). At an E_{ab} of 0.066 kWh mol^{-1}, our cell operates at a j_p of 140 mA cm^{-2} while generating 0.87 M output solutions. While our system generates acid and base solutions with high salt concentration, the salt is not likely to pose a problem for most closed-loop applications, as demonstrated below for ultramafic processing. Because it effectively dilutes the salt solution by generating separate acid and base solutions, BPMED also requires water removal when used in a closed loop system, which has an additional modest energy demand but substantially increases process complexity. Critically, BPMED systems require rigorous removal of polyvalent cations from the input salt streams to avoid irreversible CEM damage, while our system can tolerate polyvalents with periodic polarity reversals. Recently reported acid-base generating cells for CO_2 capture and slaked lime production have exhibited either substantially higher energy demand and/or even lower j_p than BPMED(*8*, *11*–*13*, *26*, *27*). In addition, some of these systems have shown rapid and irreversible voltage decay arising from incompatibility with polyvalent cations (see table S1).

Practical application of the acid-base generating strategy described above requires a way to combine cells into a stack such that H_2 generated at the cathode of one cell is utilized at the anode of the adjacent cell. We hypothesized that cells could be stacked using a bipolar gas diffusion electrode (BPGDE), which combines an HER GDE cathode and an HOR GDE anode back-to-back so that H_2 can be transported easily from one electrode to the other (Fig. 3A). A previous report demonstrated the

https://doi.org/10.26434/chemrxiv-2023-5tndz **ORCID:** https://orcid.org/0000-0003-2327-2511 Content not peer-reviewed by ChemRxiv. **License:** CC BY-NC-ND 4.0

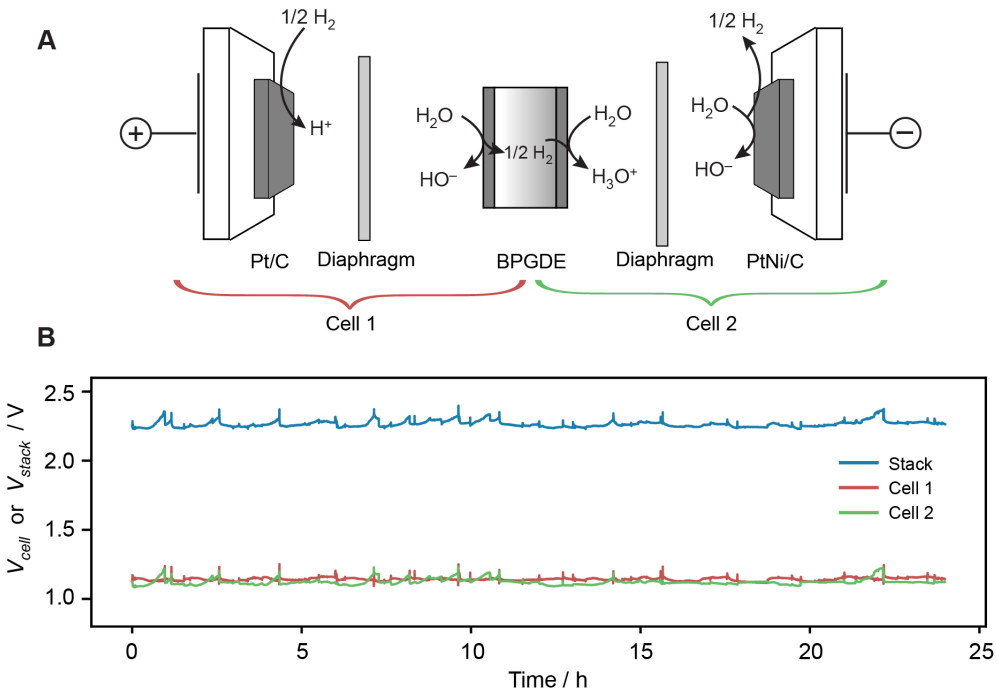

Fig. 3 **A**. Schematic of a two-cell acid-base generating stack with a BPGDE linking the cells. **B**. Voltage vs time trace for 24 h of operating the stack with mixed 3 M NaCl + 0.75 M Na_2SO_4 electrolyte at $j = 100$ mA cm^{-2}, $Q = 0.1$ mL min^{-1} cm^{-2}. Shown are the full stack voltage and the voltages of the individual cells. The BPDGE was pre-loaded with H_2 by brief polarization prior to the start but no additional H_2 was supplied over the course of the 48 h run.

use of a BPGDE as a substitute for an IEM whereby H^+ was transported from one acidic compartment to another by the HER/HOR combination. This prior construct was unable to function without supplying additional current to the cathodic half of the BPGDE only, producing excess H_2 to make up for poor hydrogen crossover efficiency from cathode to anode(*28*). To be used as a stack element for acid-base generation with our cell design, the BPGDE must generate a large pH gradient, and the H_2 generated at the cathode side must be consumed at the anode side with very high efficiency to avoid large parasitic energy losses associated with supplying makeup H_2.

We made a BPGDE by sandwiching a GDE cathode and GDE anode between two bipolar half-plates (fig. S3). The BPGDE then served as the bipolar element for the simple two-cell stack depicted in Fig. 3A. Prior to operating the stack, the BPGDE was pre-filled with H_2 by connecting potentiostat contacts to the terminal anode and BPGDE and applying a brief fixed potential. The stack was then operated at $j_{tot} =$ 100 mA cm^{-2} (200 mA total current) and $Q = 0.1$ mL min^{-1} cm^{-2} using the mixed NaCl+Na_2SO_4 electrolyte. Fig. 3B shows the voltage vs. time traces for the stack and the two component cells after an initial break-in period of 24 hours. The stack voltage maintained a quasi-steady state value of 2.25 V, and voltage spikes are attributed to

https://doi.org/10.26434/chemrxiv-2023-5tndz **ORCID:** https://orcid.org/0000-0003-2327-2511 Content not peer-reviewed by ChemRxiv. **License:** CC BY-NC-ND 4.0

concomitant bubble accumulation and release. The CE was determined by $Mg(OH)_2$ precipitation to be 69% during both the break-in period and the quasi-steady-state period, which is comparable to the performance of a single cell. Critically, the ability of the BPGDE to operate with no external H_2 supply for 48 h indicates that at least 99.99% of the H_2 generated at the BPGDE's cathode is oxidized at the connected anode. The minimal H_2 loss to the flowing electrolyte is attributed to the high ionic strength of the BPGDE cathode environment, which further limits the already low solubility of H_2 in water.

Ultramafic Rock Processing

Olivine (Mg endmember: Mg_2SiO_4) and serpentine (Mg endmember: $Mg_3Si_2O_5(OH)_4$) are attractive resources for CO_2 removal because of their abundance (*29*–*31*) and high MgO content. While the reaction of these minerals with CO_2 to form Mg carbonates is thermodynamically favored(*32*), it is extremely slow under ambient conditions and limited to low conversions because of passivation phenomena(*33*, *34*). Acidic leaching of Mg^{2+} followed by alkaline precipitation provides a way to extract the alkalinity from olivine and serpentine in the form of $Mg(OH)_2$(*1*, *35*), which can react with CO_2 under ambient conditions at useful rates(*36*, *37*). The acid and base solutions generated by our cell were therefore evaluated for their ability to process olivine and serpentine for this purpose (Fig. 4A and B).

To process olivine, the anolyte output from the extended single-cell run described above (Fig. 2F) was combined with 5 molar equivalents of olivine sand ($Mg_{2-x}Fe_xSiO_4$;, x∼0.1, see table S3), where 1 equivalent corresponds to 1 $Mg_{2-x}Fe_xSiO_4$ per 4 H^+ in the anolyte (HSO_4^- + H_3O^+). The suspension was stirred until the solution pH rose to >2.5, which took ∼48 h, and then separated from the remaining olivine by filtration. Since olivine dissolves congruently in acid (*38*), the contacted anolyte solution at this point contains Mg^{2+}, Fe^{2+}, soluble silicic acid (H_4SiO_4), other metal ion impurities, and the electrolyte components (table S4). To remove the Fe, Si, and other impurities (*39*–*41*), the catholyte was added drop-wise to reach pH∼8 and the resulting dark precipitate was separated by filtration. Analysis by SEM-EDX indicated that it is composed predominantly of Si, Fe, and Mg compounds, with a 10:2.3:1.0 Si:Fe:Mg ratio (fig. S4). The filtrate was then combined with additional catholyte to increase the pH to ∼10, which resulted in a white precipitate that was confirmed by powder XRD (pXRD) to be $Mg(OH)_2$ (Fig. 4C). SEM-EDX analysis showed that only trace amounts of Si (<1 mol%) and no Na, Cl, S or other elements were detected, indicating nearly complete recovery of electrolyte for continued electrolysis (fig. S5).

In addition to this batch experiment, we confirmed that the dissolution of olivine can be performed continuously by flowing an acidic electrolyte through a bed of olivine sand (fig. S6). By adding olivine as it is dissolved and controlling the flow rate, it is possible to achieve both high proton consumption and essentially quantitative consumption of the olivine with this simple design.

In contrast to olivine, acid digestion of serpentine, a phyllosilicate, only releases the cations and trace amounts of Si species, leaving behind an insoluble, amorphous silica passivation layer that inhibits further dissolution (*42*). Previous reports have used energy-intensive ball milling or grinding to remove the passivation layer(*43*, *44*). We found that the silica passivation is removed in alkaline solutions (>0.1 M NaOH)

https://doi.org/10.26434/chemrxiv-2023-5tndz **ORCID:** https://orcid.org/0000-0003-2327-2511 Content not peer-reviewed by ChemRxiv. **License:** CC BY-NC-ND 4.0

under ambient conditions to form soluble silicate species (e.g., Na_2SiO_3). We therefore

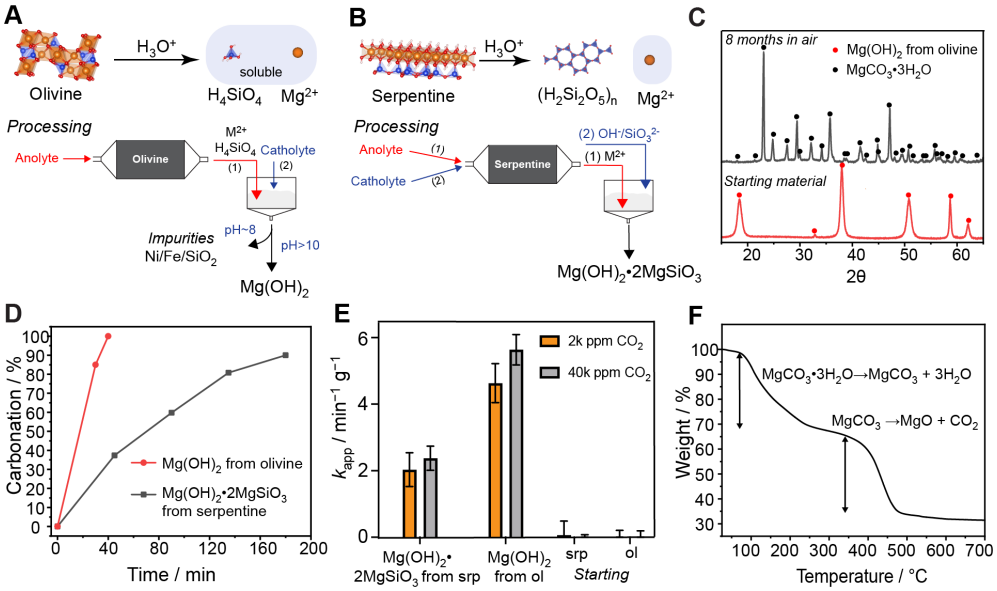

Fig. 4 Ultramafic processing and CO_2 removal A. Schematics of acid dissolution and processing method for olivine. Orange, blue, red and pink represent Mg, Si, O and H. **B**. Schematics of acid dissolution and processing method for serpentine. **C**. pXRD of $Mg(OH)_2$ obtained from olivine processing and its carbonated product after 8 months in air under wet conditions at ambient temperature. **D**. Extent of carbonation vs. time for $Mg(OH)_2$ obtained from processing olivine and $Mg(OH)_2 \cdot 2\,MgSiO_3$ obtained from processing serpentine **E**. Apparent 2nd order rate constants for uptake of CO_2 from dilute streams for $Mg(OH_2$ obtained from processing olivine (ol) and $Mg(OH)_2 \cdot 2\,MgSiO_3$ obtained from processing serpentine (srp). Starting ol and srp showed no measurable uptake **F**. TGA of magnesium carbonate product from the carbonation of $Mg(OH)_2$ obtained from olivine in air for 8 months.

developed a procedure to process serpentine consisting of alternating acid (anolyte) and base (catholyte) treatments. For a batch experiment, anolyte was stirred with 5 molar equivalents of ground serpentine until the pH rose to ∼2.5 and then separated by filtration. SEM/EDX analysis indicated a decrease in the Mg:Si ratio of the serpentine after this step and pXRD analysis showed no crystalline SiO_2 phase, which are consistent with the accumulation of an amorphous SiO_2 passivation layer (fig. S7). Instead of adding the catholyte directly to the contacted anolyte at this point, the catholyte was added to the serpentine to dissolve the SiO_2 layer as a silicate solution. The anolyte and catholyte were then combined, yielding a white precipitate. SEM/EDX showed relatively large particles (100-400 µm) with Mg and Si as the only major cations detected, and pXRD showed only very broad, low-intensity peaks that could not be definitively assigned (fig. S8). Thermogravimetric analysis (TGA) showed a sharp mass loss at 300 °C - 500 °C, which is characteristic of $Mg(OH)_2$ dehydration.

https://doi.org/10.26434/chemrxiv-2023-5tndz **ORCID:** https://orcid.org/0000-0003-2327-2511 Content not peer-reviewed by ChemRxiv. **License:** CC BY-NC-ND 4.0

Based on the ratio of this mass loss to the residual mass, the approximate composition of the precipitated material can be assigned as $Mg(OH)_2 \cdot 2\,MgSiO_3$, which is the expected composition assuming that the NaOH in the catholyte quantitatively removes the amorphous silica formed from the acidic Mg^{2+} leaching. (fig. S9)

The reactivities of solids obtained from acid/base processing were compared to the parent minerals by performing carbonation reactions in which 5 wt% slurries of each solid were stirred under 1 atm CO_2 at ambient temperature. Under these conditions, carbonation produces soluble $Mg(HCO_3)_2$. The extent of carbonation was assessed by periodic analysis of the supernatant (see Supplementary Materials). The $Mg(OH)_2$ obtained from olivine fully carbonated into soluble $Mg(HCO_3)_2$ in 45 min, forming a clear solution. The carbonation of $Mg(OH)_2 \cdot 2\,MgSiO_3$ obtained from serpentine demonstrated slower kinetics, but still reached >90% carbonation in 4 h (Fig. 4D). By contrast, no carbonation was observed for olivine or serpentine under the same conditions. The complete lack of carbonation reactivity for olivine was also confirmed by IR and TGA analysis (fig. S10).

To compare reactivity at lower partial pressures, the CO_2 uptake kinetics of the various rock samples were also measured in CO_2 absorption experiments for 30 wt% CDR material slurries with CO_2 concentrations of 2,000 and 40,000 ppm (Fig. 4E). The apparent rate constants, k_a, provide a quantitative descriptor to compare the carbonation reactivity of alkaline solids. Carbonation rates were found to be roughly first order in CO_2, with second-order apparent rate constants of 5.6 min^{-1} g^{-1} and 2.4 min^{-1} g^{-1} found for olivine-derived $Mg(OH)_2$ and serpentine-derived $Mg(OH)_2 \cdot 2\,MgSiO_3$, whereas rates of uptake were negligible for olivine and serpentine themselves. Finally, the carbonation of olivine-derived $Mg(OH)_2$ was also tested in ambient air. The solid was kept under wet conditions by adding 1g H_2O/g material daily. The progress of the carbonation was tracked by analyzing solid content by pXRD. $Mg(OH)_2$ was converted into magnesite ($MgCO_3 \cdot 3\,H_2O$) in 8 months (Fig. 4C and F).

The foregoing studies emphasize the power of electrolyte design in enabling high-efficiency acid-base generation without the need for ion-exchange membranes. The studies also evince the viability of using reversible hydrogen electrocatalysis to drive acid-base formation with minimal H_2 loss in a stack configuration and the use of the resulting acid-base equivalents to convert olivines and serpentines to active materials for irreversible CO_2 removal. By exploiting electrolyte non-idealities and binding acid or base equivalents, the principles outlined here could be extended to furnish acid-base solutions tailor-made for close-loop resource recovery and material processing powered by renewable electricity.

Acknowledgement This work was supported by the Solar Photochemistry and Catalysis Programs of the Chemical Sciences, Geosciences, and Biosciences Division, Office of Basic Energy Sciences, US Department of Energy, DE-SC0021633, the Accelerated Decarbonization Program of the Canadian Institute for Advanced Research, and the Stanford Woods Institute for the Environment. Part of this work was performed at the Stanford Nano Shared Facilities (SNSF), supported by the National Science Foundation under award ECCS-2026822. J.G.W. is supported by a Stanford Graduate Fellowship and B.P.C. is supported by a Chevron Fellowship in Energy.

Supplementary Materials

Materials and Methods

https://doi.org/10.26434/chemrxiv-2023-5tndz **ORCID:** https://orcid.org/0000-0003-2327-2511 Content not peer-reviewed by ChemRxiv. **License:** CC BY-NC-ND 4.0

Supplementary Text
Figs. S1 to S10
Tables S1 to S4

References

1. A. Azdarpour *et al.*, *Energy Procedia* **61**, 2783–2786 (2014).
2. S. E. Renfrew, D. E. Starr, P. Strasser, *ACS catalysis* **10**, 13058–13074 (2020).
3. G. H. Rau *et al.*, *Proceedings of the National Academy of Sciences* **110**, 10095–10100 (2013).
4. E. National Academies of Sciences, Medicine, *et al.*, *A research strategy for ocean-based carbon dioxide removal and sequestration*.
5. R. Pärnamäe *et al.*, *Journal of Membrane Science* **617**, 118538, ISSN: 0376-7388, (2023; https://www.sciencedirect.com/science/article/pii/S0376738820311157) (Jan. 1, 2021).
6. N. Agmon, *Chemical Physics Letters* **244**, 456–462, ISSN: 0009-2614, (2023; https://www.sciencedirect.com/science/article/pii/000926149500905J) (Oct. 13, 1995).
7. S. A. Mareev *et al.*, *Journal of Membrane Science* **603**, 118010, ISSN: 0376-7388, (2023; https://www.sciencedirect.com/science/article/pii/S0376738820305895) (May 15, 2020).
8. P. Zhu *et al.*, *Nature* **618**, Number: 7967 Publisher: Nature Publishing Group, 959–966, ISSN: 1476-4687, (2023; https://www.nature.com/articles/s41586-023-06060-1) (June 2023).
9. I. A. Digdaya *et al.*, *Nature Communications* **11**, Number: 1 Publisher: Nature Publishing Group, 4412, ISSN: 2041-1723, (2023; https://www.nature.com/articles/s41467-020-18232-y) (Sept. 4, 2020).
10. B. A. Mowbray, Z. B. Zhang, C. T. Parkyn, C. P. Berlinguette, *ACS Energy Letters* **8**, 1772–1778 (2023).
11. Z. Zhang *et al.*, *Energy & Environmental Science* **15**, 5129–5136 (2022).
12. L. N. Lammers *et al.*, *ACS Sustainable Chemistry & Engineering* **11**, 4800–4812 (2023).
13. R. K. Miao *et al.*, *ACS Energy Letters* **8**, 4694–4701 (2023).
14. S. Mikhaylin, L. Bazinet, *Advances in Colloid and Interface Science* **229**, 34–56, ISSN: 0001-8686, (2023; https://www.sciencedirect.com/science/article/pii/S0001868615002262) (Mar. 1, 2016).
15. European Commission. Joint Research Centre. Institute for Prospective Technological Studies., *Best available techniques (BAT) reference document for the production of chlor-alkali: Industrial Emissions Directive 2010/75/EU (integrated pollution prevention and control)*. (Publications Office, LU, 2014), (2023; https://data.europa.eu/doi/10.2791/13138).
16. S. Yu *et al.*, *Journal of Membrane Science* **653**, 120510, ISSN: 0376-7388, (2022; https://www.sciencedirect.com/science/article/pii/S0376738822002575) (July 5, 2022).

https://doi.org/10.26434/chemrxiv-2023-5tndz **ORCID:** https://orcid.org/0000-0003-2327-2511 Content not peer-reviewed by ChemRxiv. **License:** CC BY-NC-ND 4.0

17. H. Jaroszek, W. Mikołajczak, M. Nowak, B. Pisarska, *DESALINATION AND WATER TREATMENT* **64**, 223–227, (2022; http://www.deswater.com/home.php) (2017).
18. S. Holze, J. Jörissen, C. Fischer, H. Kalvelage, *Chemical Engineering & Technology* **17**, _eprint: https://onlinelibrary.wiley.com/doi/pdf/10.1002/ceat.270170604, 382–389, ISSN: 1521-4125, (2023; https://onlinelibrary.wiley.com/doi/abs/10.1002/ceat.270170604) (1994).
19. R. J. Gilliam *et al.*, *Journal of The Electrochemical Society* **159**, Publisher: IOP Publishing, B627, ISSN: 1945-7111, (2023; https://iopscience.iop.org/article/10.1149/2.033206jes/meta) (Mar. 21, 2012).
20. B. A. W. Mowbray, Z. B. Zhang, C. T. E. Parkyn, C. P. Berlinguette, *ACS Energy Letters* **8**, Publisher: American Chemical Society, 1772–1778, (2023; https://doi.org/10.1021/acsenergylett.3c00242) (Apr. 14, 2023).
21. M. DeMarinis, E. S. D. Castro, R. J. Allen, K. Shaikh, US Patent, 6103077A, (2023; https://patents.google.com/patent/US6103077A/en) (2000).
22. K. G. Weil, *Berichte der Bunsengesellschaft für physikalische Chemie* **95**, _eprint: https://onlinelibrary.wiley.com/doi/pdf/10.1002/bbpc.19910951030, 1305–1305, ISSN: 0005-9021, (2023; https://onlinelibrary.wiley.com/doi/abs/10.1002/bbpc.19910951030) (1991).
23. L. Hnedkovsky, R. H. Wood, V. N. Balashov, *The Journal of Physical Chemistry B* **109**, Publisher: American Chemical Society, 9034–9046, ISSN: 1520-6106, (2023; https://doi.org/10.1021/jp045707c) (May 1, 2005).
24. Y. Tanaka, in *Membrane Science and Technology*, ed. by Y. Tanaka (Elsevier, Jan. 1, 2007), vol. 12, pp. 383–404, (2023; https://www.sciencedirect.com/science/article/pii/S0927519307120167).
25. M. Reig, S. Casas, C. Valderrama, O. Gibert, J. L. Cortina, *Desalination* **398**, 87–97, ISSN: 0011-9164, (2023; https://www.sciencedirect.com/science/article/pii/S0011916416308591) (Nov. 15, 2016).
26. H. D. Willauer, F. DiMascio, D. R. Hardy, F. W. Williams, *Industrial & Engineering Chemistry Research* **53**, Publisher: American Chemical Society, 12192–12200, ISSN: 0888-5885, (2023; https://doi.org/10.1021/ie502128x) (Aug. 6, 2014).
27. L. D. Ellis, A. F. Badel, M. L. Chiang, R. J.-Y. Park, Y.-M. Chiang, *Proceedings of the National Academy of Sciences* **117**, Publisher: Proceedings of the National Academy of Sciences, 12584–12591, (2023; https://www.pnas.org/doi/full/10.1073/pnas.1821673116) (June 9, 2020).
28. N. Furuya, M. Kawamura, N. Mineo, *Denki Kagaku* **56**, Publisher: 666–667, ISSN: 0366-9297, 2434-2556, (2023; https://www.jstage.jst.go.jp/article/kogyobutsurikagaku/56/8/56_666/_article/-char/ja/) (Aug. 5, 1988).
29. H. de Coninck, S. M. Benson, *Annual review of environment and resources* **39**, 243–270 (2014).
30. J. Pronost *et al.*, *Environmental science & technology* **45**, 9413–9420 (2011).

https://doi.org/10.26434/chemrxiv-2023-5tndz **ORCID:** https://orcid.org/0000-0003-2327-2511 Content not peer-reviewed by ChemRxiv. **License:** CC BY-NC-ND 4.0

31. T. P. Bide, M. T. Styles, J. Naden, *Transactions of the Institutions of Mining and Metallurgy, Section B: Applied Earth Science* **123**, 179–195, ISSN: 17432758 (Sept. 2014).

32. W. Oconnor, (https://www.researchgate.net/publication/315844800).

33. J. Vink, D. Giesen, E. Ahlrichs, *Olivine weathering in field trials-Effect of natural environmental conditions on mineral dissolution and the potential toxicity of nickel*, 2022.

34. H. Béarat *et al.*, *Environmental science & technology* **40**, 4802–4808 (2006).

35. A. Scott *et al.*, *Communications Earth & Environment* **2**, 25 (2021).

36. K. Rausis, A. R. Stubbs, I. M. Power, C. Paulo, *International Journal of Greenhouse Gas Control* **119**, 103701 (2022).

37. A. L. Harrison, I. M. Power, G. M. Dipple, *Environmental science & technology* **47**, 126–134 (2013).

38. E. H. Oelkers, J. Declercq, G. D. Saldi, S. R. Gislason, J. Schott, *Chemical Geology* **500**, 1–19, ISSN: 00092541 (Nov. 2018).

39. A. Scott *et al.*, *Communications Earth and Environment* **2**, ISSN: 26624435 (Dec. 2021).

40. R. W. Clark, J. M. Bonicamp, *Journal of Chemical Education* **75**, 1182 (1998).

41. G. R. Choppin, P. Pathak, P. Thakur, *Main Group Metal Chemistry* **31**, 53–72 (2008).

42. F. Bo, Y.-p. Lu, Q.-m. Feng, D. Peng, L. Na, *Transactions of Nonferrous Metals Society of China* **23**, 1123–1128 (2013).

43. G. Rim, "Coupled Kinetic and Mechanistic Study of Carbonation of Silicate Materials with Tailored Transport Behaviors for CO2 Utilization", tech. rep.

44. G. Rim, D. Wang, M. Rayson, G. Brent, A. H. A. Park, *Industrial and Engineering Chemistry Research* **59**, 6517–6531, ISSN: 15205045 (Apr. 2020).

https://doi.org/10.26434/chemrxiv-2023-5tndz **ORCID:** https://orcid.org/0000-0003-2327-2511 Content not peer-reviewed by ChemRxiv. **License:** CC BY-NC-ND 4.0